TABLE OF CONTENTS

1   INTRODUCTION

The purpose of this document is to describe the data quality of the AirMSPI L1B2 products specifically for the ObseRvations of Aerosols above CLouds and their intEractionS (ORACLES) field campaign out of Walvis Bay, Namibia, which took place over the South Atlantic Ocean off the coast of Namibia and Angola, and includes the transit flights from Palmdale, CA to Warner Robins, GA to Recife, Brazil to Walvis Bay, Namibia and back. AirMSPI imagery was acquired from 28 July to 6 October 2016.

1.1   AirMSPI L1B2 Products

The Airborne Multiangle SpectroPolarimetric Imager (AirMSPI) Level 1B2 products contain radiometric and polarimetric observations of clouds, aerosols, and the surface of the Earth made from the National Aeronautics and Space Administration's (NASA's) ER-2 high-altitude research aircraft. The AirMSPI instrument acquires data using one of two possible modes, step-and-stare and sweep. Step-and-stare data are gridded with 10 m spatial sampling, with one file provided for each view angle. Sweep data are gridded with 25 m spatial sampling. Files are distributed in HDF-EOS-5 format.

The instrument reports for eight spectral bands (355, 380, 445, 470, 555, 660, 865, and 935 nm) the incident radiance (Stokes *I*), complemented with the linear polarization state (Stokes *Q* and *U*) in three of the bands (470, 660, and 865 nm) for a total of 14 channels.

1.2   AirMSPI Data Processing and Distribution

The MISR Science Computing Facility (SCF) at the Jet Propulsion Laboratory (JPL) supports the development of AirMSPI science algorithms and software, instrument calibration and performance assessment, and also provides quality assessment and data validation services with respect to AirMSPI Science Data Processing (SDP). The MISR SCF is used to perform the standard processing of the AirMSPI data. After AirMSPI data processing is complete, the standard output products are archived and made available to users via the Langley Research Center (LaRC) Atmospheric Science Data Center (ASDC) client services.   See https://eosweb.larc.nasa.gov/project/airmspi/airmspi_table.

1.3   Controlling Documents

1) Multiangle Spectropolarimetric Imager (MSPI) Algorithm Theoretical Basis Document Rev. B Draft, November 2009 (or latest version).

1.4   Related Documents

1) AirMSPI Data Product Specification for the AirMSPI Level 1B2 Products, JPL D-100523, June 2017 (or latest version).

2) User Guide for the AirMSPI Level 1B2 Products, JPL D-78962, January 2016 (or latest version).

2 RADIOMETRIC CALIBRATION

2.1 Laboratory Calibration

Laboratory radiometric calibration of the AirMSPI instrument (Diner et al., 2013a) was conducted on 30 March 2016 (prior to the ORACLES field campaign) by observing the output port of a 1.65 m integrating sphere. The sphere illuminates the entire field of view of the instrument. Data were collected at multiple light levels and the sphere output was monitored with an Analytical Spectral Devices (ASD) FieldSpec Pro spectrometer in order to generate a digital number (DN) vs. radiance regression for each pixel. The AirMSPI line arrays have 1536 pixels in each channel. Offset levels are determined from observations in 100 pixels at the end of each array that are shielded from illumination; hence only 1436 pixels in each line collect image data. After correction for non-linearity (lincal), gain factors are computed on a per-pixel basis for each channel.

2.2 Vicarious Calibration

On 5 July 2016, AirMSPI overflew the parking lot at Hangar 703, Armstrong Research Flight Center (AFRC) in Palmdale, CA. This was the first of two engineering checkout flights, in preparation for ORACLES. Data were taken both from the air, and by a team on the ground. For the latter, both the reflectance of the parking lot, surface pressure, and aerosol loading measurements were made. Instrumentation included an ASD field spectrometer and a Microtops II sunphotometer. These data were used as input to a Markov chain radiative transfer code, which calculates top-of-atmosphere spectral radiances. The Markov chain code is a vector code, tracing polarization components through the atmosphere (Xu et al., 2010). This vicarious calibration of AirMSPI had band-dependent agreement with the laboratory calibration. Differences ranged from 15% in the UV to 1% in the mid-visible. The radiometric calibration of AirMSPI for the ORACLES campaign was set using this vicarious calibration. It is believed to have a higher accuracy than the laboratory calibration, due to the low UV light levels used to calibrate AirMSPI in the laboratory.

2.3 Calibration Traceability

AirMSPI calibrations are traceable to *Système international* (SI) Units, via National Institute of Standards and Technology (NIST) standards. For laboratory calibrations, this is through a reference 20.32 cm (8 inch) integrating sphere, calibrated annually by the vendor, Gooch & Housego (http://goochandhousego.com/). For vicarious calibrations, this is through a Spectralon reflectance standard located at the vicarious calibration site.

2.4 Radiometric Data Quality Indicators

Following the practice adopted by the Multi-angle Imaging SpectroRadiometer (MISR) project, each AirMSPI pixel is assigned a Radiometric Data Quality Indicator (RDQI). The RDQI definitions are as follows:

RDQI = 0: No radiometric issues are identified.

RDQI = 1: The radiometric quality does not meet an identified threshold but is deemed usable for scientific analysis purposes.

RDQI = 2: The radiometric quality does not meet a secondary threshold and the data from this pixel should not be used for scientific analysis purposes.

RDQI = 3: The quality of the pixel is scientifically and cosmetically unusable. In addition, the shielded pixels at the end of each line array are marked with an RDQI of 3.

During laboratory calibration, a "gain" is computed from the slope of camera output DN to total-band incident radiance, *I*. It is observed that pixels with a large out-of-band leakage have a larger uncertainty in this gain, in that it is observed to vary with the spectrum of the incident light. A data quality indicator can thus be computed based on the change in gain with different illumination sources. Specifically, we take the ratio of the gain computed with an incandescent lamp to the gain computed from adding a UV plasma lamp. Pixels for which this gain ratio is between 0.95 and 1.05 are assigned an RDQI value of 0 indicating that out-of-band light is a small contributor to the measured radiance. Pixels for which the gain ratio is outside of this range, but between 0.90 and 1.10 are assigned an RDQI value of 1. Pixels with gain ratios outside both these ranges, but between 0.80 and 1.20 are assigned an RDQI value of 2. All other pixels are assigned an RDQI value of 3. The observed out-of-band leakage is believed to be the cause of permanent striping in the images, which is particularly noticeable in the UV bands.

Pixels marked with RDQI = 0 are expected to have an absolute radiometric uncertainty of ~5% (1σ). This radiometric uncertainty is attributed to the vicarious calibration methodology, which sets the absolute radiometric scale. The laboratory calibration is used to establish the relative-pixel response, also known as "flat-fielding". Comparisons of radiometric laboratory calibrations before (30 March 2016) and after (19 January 2017) ORACLES suggest that the sensor remained stable during the campaign. The pre-campaign laboratory calibration was applied to the campaign data, because the quality of the post-campaign calibration is reduced due to a striping issue that developed during the campaign (see Section 6).

3   SPECTRAL CALIBRATION

Determination of the detailed spectral response function (SRF) of each AirMSPI channel has been made based on the laboratory calibration of 9 December 2013. A monochromator was used for this purpose. The SRF is equal to the camera response to monochromatic light normalized by a silicon diode response. The monochromator provided wavelength scans from 300 to 2500 nm. Two sources were used in separate spectral scans of all channels — a Luxim Light Emitting Plasma lamp for ultraviolet-blue, and a quartz-halogen lamp for the remaining visible and near-infrared channels. The results of this calibration are shown in Table 1 and Figure 2.

In the current product release (V006), center wavelengths, effective (equivalent square-band) bandwidths, and effective (equivalent square-band) transmittances are calculated by applying the moments method of Palmer (1984) to the normalized spectral response of each band over the

range 300-1100 nm. Solar irradiances are weighted by the total-band spectral response. The Wehrli (1985) extraterrestrial solar spectrum was used for this purpose. These values are provided in Table 1 below, and represent the total-band response.

In general, radiometric response at wavelengths far from the "in-band" spectral region is estimated at $< 10^{-4}$ of the peak response, though as noted above, a larger amount of out-of-band leakage is present in a small subset of pixels in the UV bands, leading to striping in a portion of the UV images. Currently uncorrected striping in the 355 and 380 nm bands is attributed to filter blemishes that create a scene-dependent scattered light response.

Table 1 – Total-band effective center wavelength, bandwidth and transmittance, and total-band weighted solar irradiance E_0 [W m^{-2} nm^{-1}] at 1 AU

| Channel Name	Center Wavelength (nm)	Effective Bandwidth (nm)	Effective Transmittance	Solar Irradiance (W m^{-2} nm^{-1})
355I	355.1	47.7	0.609	1.002
380I	377.2	40.4	0.750	1.079
445I	443.3	46.0	0.799	1.861
470I	469.1	45.5	0.824	2.000
470Q	469.4	45.0	0.837	1.999
470U	468.8	46.0	0.815	2.000
555I	553.5	38.6	0.758	1.857
660I	659.2	45.2	0.835	1.555
660Q	659.1	43.8	0.881	1.556
660U	659.1	48.2	0.798	1.556
865I	863.3	43.5	0.829	0.976
865Q	863.7	45.6	0.810	0.976
865U	864.1	48.5	0.753	0.975
935I	931.3	53.2	0.809	0.823
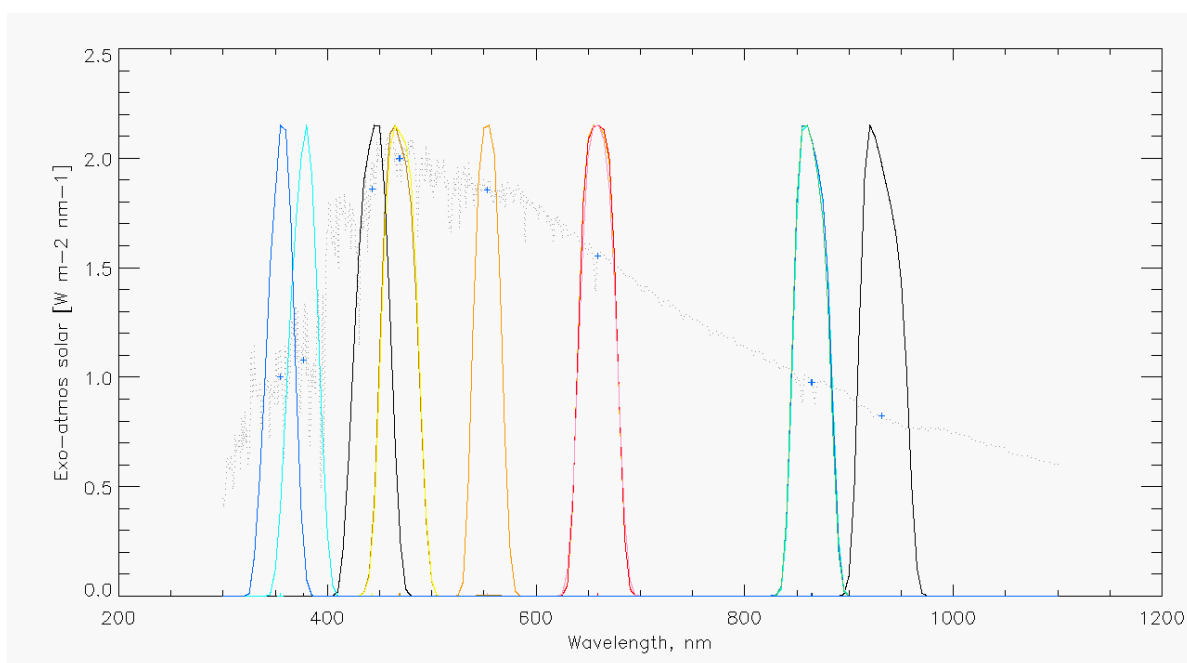
Figure 2. AirMSPI spectral response functions (SRF) shown in colored lines with the Wehrli (1985) exoatmospheric solar irradiance values shown in the faint, gray, dotted line. E0 values at 1 AU are indicated by the "+" symbol.

4   POLARIMETRIC CALIBRATION

AirMSPI uses a time-varying retardance in the optical path to modulate the orientation of the linearly polarized component of the incoming light, described by the Stokes components Q (excess of horizontally over vertically polarized light) and U (excess of 45º over 135º polarized light) (Diner et al., 2007, 2010; Mahler et al., 2011). As a result, the ratios of these parameters to the radiance I, given by $q = Q/I$ and $u = U/I$ are to first order insensitive to the absolute radiometric calibration of a given pixel because both the numerator and denominator are determined from signals acquired by the same detector element. The degree of linear polarization (DOLP) and angle of linear polarization (AOLP) derived from these ratios, equal to $\sqrt{q^2 + u^2}$ and $0.5\tan^{-1}(u/q)$, respectively, are likewise insensitive to absolute radiometric calibration, based on similar considerations. To compensate for instrumental polarization aberrations (e.g., mirror diattenuation, imperfect retardance), a set of 10 polarimetric calibration coefficients is established for every pixel (Diner et al., 2010).

Two specialized pieces of equipment exist for verifying and controlling the performance of the polarimetric measurement approach during in-flight operations of AirMSPI. The first is an optical probe, which continuously sends a beam of light through the PEMs to monitor their retardances and phases. The information from the probe shows how far the PEM retardances and phases are from their desired values. A feedback control system within the instrument then adjusts the PEM parameters to drive the error signals to zero. Test data demonstrated the ability to control the PEM retardance and phase parameters to within a fraction of 1 mrad, keeping contributions to the overall DOLP uncertainty budget at <0.001. The second polarization monitoring system is an external polarization validator, which consists of nine light-emitting

5

diodes (LEDs), three each at the AirMSPI polarimetric bands, that illuminate a plastic diffuser. In front of the diffuser, sheet polarizers are placed in different orientations. The validator is viewed before and after every multiangle observation of an Earth scene. Information from the validator system is used to derive instrument dark current and evaluate the stability of the DOLP measurements.

Results from a ground-based version of the instrument, GroundMSPI (Diner et al., 2012), show systematic DOLP uncertainties (excluding the effects of random noise), determined as the root-mean-square residual in DOLP as a polarizer is rotated in front of the camera, of ±0.003 or better. Results for AirMSPI, using the rotating polarizer methodology described in Diner et al. (2010), show similar residuals.

5   GEORECTIFICATION AND CO-REGISTRATION

As a part of the ground data processing, AirMSPI data from all spectral bands and all viewing angles are georectified and co-registered to a common Earth-based, Universal Transverse Mercator (UTM) projection grid. Distortions that can be associated with AirMSPI's type of pushbroom remote sensing imaging are taken into account by properly defining instantaneous pixel projection rays using ancillary data such as estimates of camera internal viewing geometry and ER-2 navigation data, which provide dynamic measures of the platform altitude and attitude variations. There are two types of AirMSPI georectified data products: 1) terrain projected and 2) ellipsoid projected. Terrain-projected data use a digital elevation model (DEM) for the projection surface so that cloud-free imagery is truly orthorectified with reference to that surface. Ellipsoid-projected data use the World Geodetic System 1984 (WGS84) Earth reference ellipsoid for the projection surface. One purpose of the ellipsoid projection is to provide input to stereoscopic height retrievals for predominantly cloudy imagery. Automatic stereoscopic retrieval software is currently in development.

Factors affecting geospatial accuracy of AirMSPI products include: 1) relative band-to-band co-registration within a single viewing angle, 2) multi-angle co-registration, and 3) absolute georectification. The uncertainty depends on the magnitude of the errors in the supplied ancillary data and errors in the projection surface defined by the DEM. In the case of the ORACLES campaign, most data are acquired entirely over the ocean surface and therefore processed into ellipsoid-projected data products only. For the remainder of data sets acquired over land a terrain-projected data product is also derived based on a JPL internal version of the Shuttle Radar Topography Mission (SRTM) Plus (SRTMv3 60n-60s; ASTERv2 60n-83s; RAMP 60s-90s; JPL-LRR020977) with 30 m horizontal postings. Errors in the ancillary data defining viewing geometry are handled as static and dynamic pointing errors in order to characterize them using available ground control points (GCPs) in a procedure based on simultaneous bundle adjustment (Jovanovic et al., 2012). For targets where there is an optimum number of GCPs available, both static and dynamic pointing errors are recovered simultaneously prior to georectification and co-registration. These data are denoted as having full geometric calibration "directly" applied with expected co-registration and georectification uncertainty of around 15 m rms across all viewing angles and all bands. For other targets, (i.e., those without available GCPs, which are mostly fully ocean or cloudy imagery), an estimate of static pointing errors made on separate flight lines within the same campaign is utilized. These products are denoted as having geometric calibration

"indirectly" applied with a current estimate of georectification and co-registration uncertainty of less than one hundred meters. The type of geometric calibration is recorded in the file metadata list under the field name "Geolocation stage". Analysis and implementation efforts are still in progress with an objective to fully optimize the camera viewing model so that uncertainties of indirectly calibrated data are minimized.

Band-to-band relative co-registration uncertainty within the same viewing angle is well within 10 m, which is the pixel size of the map projection grid in the step-and-stare terrain-projected data. In the case of ellipsoid-projected data there will be some offsets in the relative band-to-band registration due to the parallax caused by the true height of the viewing surface and physical band separation in the focal plane. Additionally, slight errors in registration can cause a small displacement (on the order of a degree or two) of polarimetric features such as the backscatter glory from their expected location.

Occasional gaps of isolated lines in AirMSPI pushbroom imagery are present in ~2% of the images (listed in Appendix B). These are due to changes in the ER-2 pitch attitude that occurred too abruptly (e.g., as the result of turbulence) to either: 1) be captured accurately in the ER-2 navigation data, and/or 2) cause occasional gaps in the imagery created in the pushbroom fashion.

6   INCIDENTAL DATA QUALITY ISSUES

During the ORACLES campaign, a poor connector contact caused striping in the images in the along-track direction. The number of detector pixels that were affected increased during the campaign, and their positions changed over time. Moreover, the occurrence is dependent on the scene brightness, resulting in broken stripes or isolated, seemingly bright ("hot") pixels in L1B2 imagery. Those pixels are readily identifiable due to their anomalous appearance. Comparisons of radiometric and polarimetric laboratory calibrations before and after the campaign showed that the instrument response outside the affected L1B2 pixels did not change. The corrupted L1B2 data are not recoverable. Future versions of the science data may flag or mask these situations.

Care is taken to filter out corrupted data in the shielded pixels and on-board validator images which are used for in-flight calibration, in order not to contaminate the science data. In extremely rare cases (the eight images listed below), the shielded pixels themselves were affected by the bright anomalies, which introduced across-track striping upon subtraction. Those frames are readily identifiable due to their anomalous appearance. The corrupted L1B2 data are not recoverable. Future versions of the science data may flag or mask these situations.

Across-track striping has been observed in the following 8 images:
AirMSPI_ER2_GRP_ELLIPSOID_20160916_090610Z_SouthAtlanticOcean-14S9E_478A_V006
AirMSPI_ER2_GRP_ELLIPSOID_20160916_092416Z_SouthAtlanticOcean-12S9E_SWPF_V006
AirMSPI_ER2_GRP_ELLIPSOID_20160916_092943Z_SouthAtlanticOcean-11S9E_291A_V006
AirMSPI_ER2_GRP_ELLIPSOID_20160916_104943Z_SouthAtlanticOcean-9S4E_478F_V006
AirMSPI_ER2_GRP_ELLIPSOID_20160916_105036Z_SouthAtlanticOcean-9S4E_291F_V006
AirMSPI_ER2_GRP_ELLIPSOID_20160916_110513Z_SouthAtlanticOcean-9S3E_478A_V006

AirMSPI_ER2_GRP_ELLIPSOID_20160916_110607Z_SouthAtlanticOcean-9S3E_589A_V006
AirMSPI_ER2_GRP_ELLIPSOID_20160916_110705Z_SouthAtlanticOcean-9S3E_661A_V006

7 REFERENCES

Diner, D.J., A. Davis, B. Hancock, G. Gutt, R.A. Chipman, and B. Cairns (2007). Dual photoelastic modulator-based polarimetric imaging concept for aerosol remote sensing. *Appl. Opt.* **46**, 8428-8445.

Diner, D.J., A. Davis, B. Hancock, S. Geier, B. Rheingans, V. Jovanovic, M. Bull, D.M. Rider, R.A. Chipman, A. Mahler, and S.C. McClain (2010). First results from a dual photoelastic modulator-based polarimetric camera. *Appl. Opt.* **49**, 2929-2946.

Diner, D.J., F. Xu, J.V. Martonchik, B.E. Rheingans, S. Geier, V.M. Jovanovic, A. Davis, R.A. Chipman, and S.C. and McClain (2012). Exploration of a polarized surface bidirectional reflectance model using the Ground-based Multiangle SpectroPolarimetric Imager. *Atmosphere* **3**, 591-619.

Diner, D.J., F. Xu, M.J. Garay, J.V. Martonchik, B.E. Rheingans, S. Geier, A. Davis, B.R. Hancock, V.M. Jovanovic, M.A. Bull, K. Capraro, R.A. Chipman, and S.C. McClain (2013a). The Airborne Multiangle SpectroPolarimetric Imager (AirMSPI): a new tool for aerosol and cloud remote sensing. *Atmos. Meas. Tech.* **6**, 2007-2025.

Diner, D.J., M.J. Garay, O.V. Kalashnikova, B.E. Rheingans, S. Geier, M.A. Bull, V.M. Jovanovic, F. Xu, C.J. Bruegge, A. Davis, K. Crabtree, and R.A. Chipman (2013b). Airborne Multiangle SpectroPolarmetric Imager (AirMSPI) observations over California during NASA's Polarimeter Definition Experiment (PODEX). *SPIE Proc.* **8873**, 88730B-2.

Jovanovic, V.M., M. Bull, D.J. Diner, S. Geier, and B. Rheingans (2012). Automated data production for a novel Airborne Multiangle SpectroPolarimetric Imager (AirMSPI). *Int. Arch. Photogramm. Remote Sens. Spatial Inf. Sci.*, **XXXIX-B1**, 33-38.

Mahler, A., D.J. Diner, and R.A. Chipman (2011). Analysis of static and time-varying polarization errors in the multiangle spectropolarimetric imager. *Appl. Opt.* **50**, 2080-2087.

Palmer, J.M. (1984). Effective bandwidths for LANDSAT-4 and LANDSAT-D' Multispectral Scanner and Thematic Mapper subsystems. *IEEE Trans. Geosci. Rem. Sens.* **GE-22**, 336-338.

Wehrli, C. (1985). "Extraterrestrial Solar Spectrum", Publication no. 615, Physikalisch Meteorologisches Observatorium + World Radiation Center (PMO/WRC) Davos Dorf, Switzerland, July 1985.

Xu, F., A.B. Davis, R.A. West, and L.W. Esposito (2010). Markov chain formalism for polarized light transfer in plane-parallel atmospheres, with numerical comparison to the Monte Carlo method, *Opt. Express* **19**, 946-967.

8   APPENDIX A

Acronym List:

AFRC	Armstrong Flight Research Center
AirMSPI	Airborne Multiangle SpectroPolarimetric Imager
AOLP	Angle of Linear Polarization
ASD	Analytical Spectral Devices
ASDC	Atmospheric Science Data Center
AVIRIS	Airborne Visible/Infrared Imaging Spectrometer
AU	Astronomical Unit
DEM	Digital Elevation Model
DN	Digital Number
DOLP	Degree of Linear Polarization
EOS	Earth Observing System
GCP	Ground Control Point
HDF-EOS	Hierarchical Data Format for EOS
JPL	Jet Propulsion Laboratory
LaRC	Langley Research Center (NASA)
LED	Light Emitting Diode
MISR	Multi-angle Imaging SpectroRadiometer
NASA	National Aeronautics and Space Administration
NED	National Elevation Dataset
NIST	National Institute of Standards and Technology
ORACLES	ObseRvations of Aerosols above CLouds and their intEractionS
RDQI	Radiometric Data Quality Indicator
SCF	Science Computing Facility
SDP	Science Data Processing
SI	*Système international*
SRF	Spectral Response Function
SRTM	Shuttle Radar Topography Mission
USGS	United States Geological Survey
UTM	Universal Transverse Mercator
UV	Ultraviolet
WGS84	World Geodetic System 1984

9 APPENDIX B

Images containing across-track striping due to georectification:

AirMSPI_ER2_GRP_ELLIPSOID_20160826_134331Z_SouthAtlanticOcean-20S1E_661F_V006
AirMSPI_ER2_GRP_ELLIPSOID_20160826_150932Z_SouthAtlanticOcean-22S10E_661A_V006
AirMSPI_ER2_GRP_ELLIPSOID_20160910_102233Z_SouthAtlanticOcean-10S7E_661A_V006
AirMSPI_ER2_GRP_ELLIPSOID_20160910_102716Z_SouthAtlanticOcean-11S6E_661F_V006
AirMSPI_ER2_GRP_ELLIPSOID_20160910_105306Z_SouthAtlanticOcean-13S5E_478F_V006
AirMSPI_ER2_GRP_ELLIPSOID_20160910_110845Z_SouthAtlanticOcean-15S5E_478F_V006
AirMSPI_ER2_GRP_ELLIPSOID_20160912_091608Z_SouthAtlanticOcean-13S9E_478F_V006
AirMSPI_ER2_GRP_ELLIPSOID_20160912_091700Z_SouthAtlanticOcean-13S9E_291F_V006
AirMSPI_ER2_GRP_ELLIPSOID_20160912_091754Z_SouthAtlanticOcean-13S9E_000N_V006
AirMSPI_ER2_GRP_ELLIPSOID_20160912_100448Z_SouthAtlanticOcean-7S9E_478F_V006
AirMSPI_ER2_GRP_ELLIPSOID_20160912_101739Z_SouthAtlanticOcean-6S9E_291F_V006
AirMSPI_ER2_GRP_ELLIPSOID_20160912_101832Z_SouthAtlanticOcean-6S9E_000N_V006
AirMSPI_ER2_GRP_ELLIPSOID_20160912_101925Z_SouthAtlanticOcean-6S9E_291A_V006
AirMSPI_ER2_GRP_ELLIPSOID_20160912_102018Z_SouthAtlanticOcean-6S9E_478A_V006
AirMSPI_ER2_GRP_ELLIPSOID_20160912_102210Z_SouthAtlanticOcean-6S9E_661A_V006
AirMSPI_ER2_GRP_ELLIPSOID_20160912_143128Z_SouthAtlanticOcean-19S9E_291F_V006
AirMSPI_ER2_GRP_ELLIPSOID_20160914_080224Z_SouthAtlanticOcean-20S10E_291A_V006
AirMSPI_ER2_GRP_ELLIPSOID_20160914_082248Z_SouthAtlanticOcean-17S10E_589F_V006
AirMSPI_ER2_GRP_ELLIPSOID_20160914_084956Z_SouthAtlanticOcean-16S10E_589F_V006
AirMSPI_ER2_GRP_ELLIPSOID_20160914_085049Z_SouthAtlanticOcean-16S10E_478F_V006
AirMSPI_ER2_GRP_ELLIPSOID_20160914_103327Z_SouthAtlanticOcean-18S9E_662A_V006
AirMSPI_ER2_GRP_ELLIPSOID_20160916_083651Z_SouthAtlanticOcean-17S9E_661F_V006
AirMSPI_ER2_GRP_ELLIPSOID_20160916_083749Z_SouthAtlanticOcean-17S9E_589F_V006
AirMSPI_ER2_GRP_ELLIPSOID_20160916_083843Z_SouthAtlanticOcean-17S9E_478F_V006
AirMSPI_ER2_GRP_ELLIPSOID_20160916_090424Z_SouthAtlanticOcean-14S9E_000N_V006
AirMSPI_ER2_GRP_ELLIPSOID_20160916_100536Z_SouthAtlanticOcean-7S9E_291A_V006
AirMSPI_ER2_GRP_ELLIPSOID_20160916_101256Z_SouthAtlanticOcean-7S8E_589F_V006
AirMSPI_ER2_GRP_ELLIPSOID_20160916_110234Z_SouthAtlanticOcean-9S3E_291F_V006
AirMSPI_ER2_GRP_ELLIPSOID_20160916_125925Z_SouthAtlanticOcean-17S7E_589A_V006
AirMSPI_ER2_GRP_ELLIPSOID_20160916_135539Z_SouthAtlanticOcean-22S12E_661F_V006
AirMSPI_ER2_GRP_ELLIPSOID_20160916_135634Z_SouthAtlanticOcean-22S12E_590F_V006
AirMSPI_ER2_GRP_ELLIPSOID_20160916_135725Z_SouthAtlanticOcean-22S12E_478F_V006
AirMSPI_ER2_GRP_ELLIPSOID_20160916_140138Z_SouthAtlanticOcean-22S12E_590A_V006
AirMSPI_ER2_GRP_ELLIPSOID_20160916_140233Z_SouthAtlanticOcean-22S12E_661A_V006
AirMSPI_ER2_GRP_ELLIPSOID_20160918_091838Z_SouthAtlanticOcean-18S11E_589A_V006
AirMSPI_ER2_GRP_ELLIPSOID_20160918_132739Z_SouthAtlanticOcean-11S4E_478F_V006
AirMSPI_ER2_GRP_ELLIPSOID_20160920_084642Z_SouthAtlanticOcean-21S10E_661A_V006
AirMSPI_ER2_GRP_ELLIPSOID_20160920_090421Z_SouthAtlanticOcean-19S10E_589F_V006
AirMSPI_ER2_GRP_ELLIPSOID_20160920_090515Z_SouthAtlanticOcean-19S10E_478F_V006
AirMSPI_ER2_GRP_ELLIPSOID_20160920_090607Z_SouthAtlanticOcean-19S10E_291F_V006
AirMSPI_ER2_GRP_ELLIPSOID_20160920_091704Z_SouthAtlanticOcean-17S10E_661F_V006
AirMSPI_ER2_GRP_ELLIPSOID_20160920_091759Z_SouthAtlanticOcean-17S10E_590F_V006
AirMSPI_ER2_GRP_ELLIPSOID_20160920_092031Z_SouthAtlanticOcean-17S10E_000N_V006
AirMSPI_ER2_GRP_ELLIPSOID_20160920_092121Z_SouthAtlanticOcean-17S10E_291A_V006
AirMSPI_ER2_GRP_ELLIPSOID_20160920_092212Z_SouthAtlanticOcean-17S10E_478A_V006
AirMSPI_ER2_GRP_ELLIPSOID_20160920_111016Z_SouthAtlanticOcean-15S9E_661F_V006

AirMSPI_ER2_GRP_ELLIPSOID_20160920_111343Z_SouthAtlanticOcean-15S9E_000N_V006
AirMSPI_ER2_GRP_ELLIPSOID_20160920_141520Z_SouthAtlanticOcean-21S9E_589F_V006
AirMSPI_ER2_GRP_ELLIPSOID_20160920_141613Z_SouthAtlanticOcean-21S9E_478F_V006
AirMSPI_ER2_GRP_ELLIPSOID_20160920_142621Z_SouthAtlanticOcean-23S9E_661F_V006
AirMSPI_ER2_GRP_ELLIPSOID_20160920_142718Z_SouthAtlanticOcean-23S9E_589F_V006
AirMSPI_ER2_GRP_ELLIPSOID_20160920_142905Z_SouthAtlanticOcean-23S9E_291F_V006
AirMSPI_ER2_GRP_ELLIPSOID_20160920_143052Z_SouthAtlanticOcean-23S9E_291A_V006
AirMSPI_ER2_GRP_ELLIPSOID_20160920_143145Z_SouthAtlanticOcean-23S9E_478A_V006
AirMSPI_ER2_GRP_ELLIPSOID_20160920_143239Z_SouthAtlanticOcean-23S9E_589A_V006
AirMSPI_ER2_GRP_ELLIPSOID_20160922_081932Z_SouthAtlanticOcean-21S11E_661A_V006
AirMSPI_ER2_GRP_ELLIPSOID_20160922_083033Z_SouthAtlanticOcean-20S10E_589A_V006
AirMSPI_ER2_GRP_ELLIPSOID_20160922_083131Z_SouthAtlanticOcean-20S10E_661A_V006
AirMSPI_ER2_GRP_ELLIPSOID_20160922_144519Z_SouthAtlanticOcean-23S12E_482A_V006
AirMSPI_ER2_GRP_ELLIPSOID_20160924_084941Z_SouthAtlanticOcean-16S11E_478F_V006
AirMSPI_ER2_GRP_ELLIPSOID_20160924_090046Z_SouthAtlanticOcean-15S11E_589F_V006
AirMSPI_ER2_GRP_ELLIPSOID_20160924_090233Z_SouthAtlanticOcean-15S11E_291F_V006
AirMSPI_ER2_GRP_ELLIPSOID_20160924_095900Z_SouthAtlanticOcean-9S11E_291A_V006
AirMSPI_ER2_GRP_ELLIPSOID_20160924_095900Z_SouthAtlanticOcean-9S11E_291A_V006
AirMSPI_ER2_GRP_ELLIPSOID_20160924_121126Z_SouthAtlanticOcean-10S3E_589F_V006
AirMSPI_ER2_GRP_ELLIPSOID_20160924_132712Z_SouthAtlanticOcean-17S7E_478F_V006
AirMSPI_ER2_GRP_ELLIPSOID_20160924_132805Z_SouthAtlanticOcean-17S7E_291F_V006
AirMSPI_ER2_GRP_ELLIPSOID_20160925_084635Z_SouthAtlanticOcean-18S9E_589F_V006
AirMSPI_ER2_GRP_ELLIPSOID_20160925_084822Z_SouthAtlanticOcean-18S9E_291F_V006
AirMSPI_ER2_GRP_ELLIPSOID_20160925_085156Z_SouthAtlanticOcean-18S9E_589A_V006
AirMSPI_ER2_GRP_ELLIPSOID_20160925_093955Z_SouthAtlanticOcean-13S9E_589A_V006
AirMSPI_ER2_GRP_ELLIPSOID_20160927_085054Z_SouthAtlanticOcean-14S9E_661F_V006
AirMSPI_ER2_GRP_ELLIPSOID_20160927_085151Z_SouthAtlanticOcean-14S9E_589F_V006
AirMSPI_ER2_GRP_ELLIPSOID_20160927_085245Z_SouthAtlanticOcean-14S9E_478F_V006
AirMSPI_ER2_GRP_ELLIPSOID_20160927_085338Z_SouthAtlanticOcean-14S9E_291F_V006
AirMSPI_ER2_GRP_ELLIPSOID_20160927_085431Z_SouthAtlanticOcean-14S9E_000N_V006
AirMSPI_ER2_GRP_ELLIPSOID_20160927_085525Z_SouthAtlanticOcean-14S9E_291A_V006
AirMSPI_ER2_GRP_ELLIPSOID_20160927_085618Z_SouthAtlanticOcean-14S9E_478A_V006
AirMSPI_ER2_GRP_ELLIPSOID_20160927_101926Z_SouthAtlanticOcean-5S9E_661F_V006
AirMSPI_ER2_GRP_ELLIPSOID_20160927_102012Z_SouthAtlanticOcean-5S9E_585F_V006
AirMSPI_ER2_GRP_ELLIPSOID_20160929_113943Z_SouthAtlanticOcean-14S4E_589A_V006
AirMSPI_ER2_GRP_ELLIPSOID_20160929_115144Z_SouthAtlanticOcean-13S3E_589A_V006
AirMSPI_ER2_GRP_ELLIPSOID_20160929_120040Z_SouthAtlanticOcean-12S2E_291F_V006
AirMSPI_ER2_GRP_ELLIPSOID_20160929_122924Z_SouthAtlanticOcean-10S1W_661F_V006
AirMSPI_ER2_GRP_ELLIPSOID_20160929_135918Z_SouthAtlanticOcean-9S11W_478A_V006
AirMSPI_ER2_GRP_ELLIPSOID_20161006_144805Z_MS-Starkville_661F_V006
AirMSPI_ER2_GRP_ELLIPSOID_20161006_150250Z_MS-IttaBena_291F_V006
AirMSPI_ER2_GRP_ELLIPSOID_20161006_155718Z_OK-Davis_589A_V006
AirMSPI_ER2_GRP_ELLIPSOID_20161006_174515Z_AZ-AshFork_661F_V006
AirMSPI_ER2_GRP_ELLIPSOID_20161006_175958Z_AZ-Kingman_291F_V006
AirMSPI_ER2_GRP_ELLIPSOID_20161006_180913Z_CA-SanBernardinoCounty_661F_V006
AirMSPI_ER2_GRP_TERRAIN_20161006_144805Z_MS-Starkville_661F_V006
AirMSPI_ER2_GRP_TERRAIN_20161006_150250Z_MS-IttaBena_291F_V006
AirMSPI_ER2_GRP_TERRAIN_20161006_155718Z_OK-Davis_589A_V006
AirMSPI_ER2_GRP_TERRAIN_20161006_174515Z_AZ-AshFork_661F_V006
AirMSPI_ER2_GRP_TERRAIN_20161006_175958Z_AZ-Kingman_291F_V006
AirMSPI_ER2_GRP_TERRAIN_20161006_180913Z_CA-SanBernardinoCounty_661F_V006